

Popular summary for:

High-frequency planetary waves in the polar middle atmosphere as seen in a data assimilation system

L. Coy, I. Stajner, A.M. da Silva, J. Joiner, R.B. Rood, S. Pawson, S.J. Lin

for submission to The Journal of the Atmospheric Sciences

The atmosphere displays a wide range of motions with different and spatial and temporal structures. Many of these disturbances can be described as Rossby waves with specific wavenumber and frequency. One example is the quasi-two-day wave, which has been detected in ground-and-space-based observations of temperature and winds in the upper stratosphere and lower mesosphere. This study presents the first evidence of such a wave in the assimilated datasets produced by NASA's Data Assimilation Office. The study examines assimilated meteorology and ozone in July 1998, showing a significant signal in all of these quantities, representing a major source of ozone variation in the stratopause region. It is shown that the wave in the ozone assimilation is in good agreement with that inferred from data of the "Polar Ozone and Aerosol Measurement (POAM)" satellite. The two-day wave in the polar region is shown to arise in conjunction with linear instabilities of the flow, since it is associated with Eliassen-Palm flux divergence in regions of negative gradients of potential vorticity.

# **High Frequency Planetary Waves in the Polar**

## **Middle Atmosphere as seen in a Data**

### **Assimilation System**

**L. Coy \***

E. O. Hulburt Center for Space Research, Naval Research Laboratory

Washington, DC

**I. Štajner    A. M. DaSilva    J. Joiner    R. B. Rood**

**S. Pawson**

**S. J. Lin**

NASA Goddard Space Flight Center, Greenbelt, Maryland, USA.

---

\*Corresponding author address: Lawrence Coy

E. O. Hulburt Center for Space Research, Naval Research Laboratory, Code 7646  
4555 Overlook Avenue SW, Washington, DC 20375-5320, USA.

Tel: (202) 404-1266 , Fax: (202) 404-8090, e-mail: coy@uap2.nrl.navy.mil

## ABSTRACT

This study examines the winter southern hemisphere vortex of 1998 using four times daily output from a data assimilation system to focus on the polar 2-day, wave number 2 component of the 4-day wave. The data assimilation system products are from a test version of the finite volume data assimilation system (fvDAS) being developed at Goddard Space Flight Center (GSFC) and include an ozone assimilation system. Results show that the polar 2-day wave dominates during July 1998 at 70°S. The period of the quasi 2-day wave is somewhat shorter than 2 days (about 1.7 days) during July 1998 with an average perturbation temperature amplitude for the month of over 2.5 K. The 2-day wave propagates more slowly than the zonal mean zonal wind, consistent with Rossby wave theory, and has EP flux divergence regions associated with regions of negative horizontal potential vorticity gradients, as expected from linear instability theory. Results for the assimilation-produced ozone mixing ratio show that the 2-day wave represents a major source of ozone variation in this region. The ozone wave in the assimilation system is in good agreement with the wave seen in the POAM (Polar Ozone and Aerosol Measurement) ozone observations for the same time period. Some differences with linear instability theory are noted as well as spectral

peaks in the ozone field, not seen in the temperature field, that may be a consequence of advection.

# 1 Introduction

The 4-day wave is a relatively common planetary-scale stratopause disturbance found mainly during the southern hemisphere winter. This high latitude wave consists of wave 1 and 2 (and some higher wavenumber) components moving at nearly the same rotational period (the time for a crest to travel around a latitude circle), about 3–4 days, so that the period of the wave 2 component is about 1.5–2 days. Many studies of the 4-day wave have focused on the wave 1 component as only daily analyses are needed to resolve the period accurately. However, modern data assimilation systems that include the stratosphere often output 4 times a day and so can be used to examine the higher frequency wave 2 component of the 4-day wave. This paper presents results of the 4-day wave seen in the temperature and ozone fields produced by a global data assimilation system during a time when the wave 2 component was dominant.

The 4-day wave has been described by Venne and Stanford (1979, 1982), Prata (1984), Lait and Stanford (1988), Randel and Lait (1991), Manney (1991), Lawrence et al. (1995), and Lawrence and Randel (1996): more references can be found in Allen et al. (1997). Most of these studies examined satellite radiances, though Manney (1991) used daily analyses from the NCEP (National Center for Environmental Prediction) data assimilation system. The wave originates near the stratopause at the level of the

stratospheric jet maximum where the latitudinal mean zonal wind shears tend to be largest. The wave is believed to be generated by barotropic and baroclinic instability, the relative importance of either process depending on the particular zonal mean wind configuration.

The linear barotropic instability problem at the stratopause germane to 4-day wave genesis was first investigated by Hartmann (1983) for idealized latitudinal zonal wind profiles. Hartmann (1983) found that instabilities could occur on both the poleward and equatorward side of jets corresponding to negative zonal mean potential vorticity gradients on both sides of the jet. The zonal phase speeds of the unstable waves were nearly equal to the mean zonal wind speed where  $\bar{q}_y$  (the zonal mean potential vorticity gradient) changed sign. This gives shorter rotational periods on the poleward side of the jet ( $\sim 4$  days) and longer rotational periods on the equatorward side of the jet ( $\sim 15$  days) because of the change in length of latitude circles around the globe, even though the phase speeds could be similar on both sides of the jet. Using a quasi-geostrophic model Hartmann (1983) also found that baroclinic effects tended to stabilize and reduce growth rates by confining the vertical extent of the region of strong latitudinal wind shear. In Hartmann (1983) both wavenumbers 1 and 2 had similar growth rates, however, another barotropic model study (Manney et al. 1988) showed that wave 2 became the more unstable mode (rather than wave 1) as the jet became more sharply

peaked. Manney et al. (1988) also showed that the waves became more dispersive (that is, the rotational period had more variation for different wave numbers) as the jet moved equatorward.

Manney and Randel (1993) used a linear quasigeostrophic model to examine unstable modes in climatological zonal mean winds, including both barotropic and baroclinic effects. They showed that both effects were necessary for realistic growth rates to occur in the zonal mean winds they studied. These results agreed with observational studies (Randel and Lait 1991) that showed strong vertical Eliassen-Palm (EP) fluxes in some 4-day wave observations. More recent work by Allen et al. (1997) highlighted the general structure of the 4-day wave in terms of the temperatures, winds, and heights associated with a potential vorticity (pv) anomaly.

Stratospheric constituents can respond to the 4-day wave as tracers if they have mean gradients in the wave region and relatively long chemical lifetimes. Using high-latitude middle atmosphere observations from UARS (Upper Atmosphere Research Satellite) Allen et al. (1997) showed a 4-day signal in ozone while Manney et al. (1998) showed a 4-day signal in water vapor and methane. Both studies modeled the tracers differently. Allen et al. (1997) calculated the linear ozone response to the observed temperature and geostrophic meridional wind signal coupled with simple photochemistry to examine the vertical structure of the ozone signal. Manney et al. (1998) used

an isentropic transport model to examine how tracers were transported from low latitudes into the wave region. Both studies showed that the 4-day wave, when active, can explain a large amount of the tracer variability near the polar stratopause.

This paper reports on the higher frequency, wave 2 component of the 4-day wave using 6 hourly output from a data assimilation system that includes output from an off-line ozone assimilation as well as the standard assimilation-produced mass and wind fields. Following a brief description of the assimilation products and analysis methods (section 2) the assimilation based 4 day wave diagnostics are presented (section 3). In addition to the ozone assimilation the 4 day wave can be seen in POAM observations (section 4).

## **2 Analysis**

This study uses assimilation products from the Data Assimilation Office (DAO) at NASA's Goddard Space Flight Center (GSFC). Output is taken from a developmental system (fvDAS: finite volume Data Assimilation System) that was run for the year 1998. This system is based on the new fvGCM (finite volume General Circulation Model) coupled with the PSAS (Physical space Statistical Analysis System) analysis system (Cohn et al. 1998) that are used together in the current DAO operation sys-

tem. As in the current DAO production system, the top analysis level is 0.4 hPa with the actually model top at 0.01 hPa, making this a good system for stratopause studies. Output from the fvDAS includes zonal and meridional winds, temperature, and geopotential heights on 36 pressure levels from 1000–0.2 hPa at a horizontal resolution of 2.5° longitude by 2° latitude. These output fields were saved every 6 hours.

Satellite radiances are the main data going into the assimilation system in the upper stratosphere levels of interest here. Until July 1998, data from the NOAA 11 and NOAA 14 TOVS (TIROS Operational Vertical Sounder) were assimilated. TOVS consists of the High-resolution Infrared Sounder (HIRS), a 20 channel IR filter-wheel radiometer, SSU (Stratospheric Sounding Unit), a 3 channel radiometer that uses a pressure-modulation technique, and MSU (Microwave Sounding Unit), a 4 channel microwave radiometer. The channels affecting the upper stratosphere are the 2 highest peaking SSU channels and HIRS channel 1. To avoid inter-satellite biases (upper stratospheric channels are not bias-corrected), the NOAA 11 SSU channels were not assimilated. After 1 July 1998, data from the NOAA 15 Advanced TOVS (ATOVS) were added to the assimilation, where the 15 channel Advanced Microwave Sounding Unit (AMSU) replaced the SSU and MSU of previous NOAA satellites. To avoid inter-satellite bias between the NOAA 15 ATOVS and the NOAA 14 SSU, the NOAA-14 SSU channels were not assimilated after 1 July 1998. The radiances were assimilated

using a 1DVAR algorithm (Joiner and Rokke 2000).

In addition to the regular assimilation system, an off-line ozone assimilation has been run for the same time period (1998) using the fvDAS winds and temperatures as input (Štajner et al. 2001). The assimilation uses satellite-based ozone observations from SBUV (Solar Backscatter Ultra-Violet) for profile information and from TOMS (Total Ozone Mapping Spectrometer) for a total column constraint. The ozone fields are available on the same grid and at the same times as the fvDAS assimilation described above.

A standard Fourier transform package was used on two dimensional longitude by time arrays to extract the eastward propagating wave components of interest at a given latitude and height. The Fourier analysis was performed monthly (120–124 points in time). The westward propagating modes consist mainly of solar tidal periods and are not shown here. Though some higher wavenumber components also show the 4-day wave, only the dominant wave 1 and wave 2 components are presented here. EP fluxes and associated heat and momentum fluxes were calculated for a given wavenumber and frequency from the zonal wind, meridional wind, and temperature Fourier coefficients along with the zonal and monthly averaged zonal winds and temperatures. The EP flux formulas were evaluated using spherical, log-pressure coordinates (see Andrews et al. 1987, equations 3.5.3a and b, page 128).

### 3 Results

The 4-day wave is easily seen in the gridded assimilation products. Fig. 1 shows longitude time sections for temperature and ozone mixing ratio at 70°S and 2 hPa for July 1998. Both fields show wave 2 features propagating eastward with periods of about 2 days. The peak-to-peak amplitude is on the order of 10 K for temperature and 1 ppmv for ozone. A comparison with independent POAM ozone observations will be given later.

Fig. 2 gives a mid-July, 2 hPa synoptic view of the South Pole where the wave 2 structure can be easily seen. The temperature field (Fig. 2a) shows two warm regions with a cold, elongated region in between, located over the pole. Both of these warm regions are also seen in the UKMO (United Kingdom Meteorological Office) stratospheric assimilation (not shown) so the warm regions are unlikely to be a DAO system artifact. However, there are differences in temperatures between the two analyses that reflect the difficulties still associated with temperature analyses near the stratopause. The Ertel potential vorticity (pv) field (Fig. 2b) shows a strong gradient associated with the main polar vortex and a weaker, inner vortex, associated with the wave 2 feature. Ozone (Fig. 2c) also shows an elongated wave 2 low ozone region near the pole. The phase of the ozone wave disturbance is somewhat east of the temperature and pv waves.

In addition, the zonal wind component (Fig. 2d) shows a wave 2 shaped region of weak winds over the pole. The zonal wind is of interest because its meridional derivative can help to create the negative regions of potential vorticity gradient,  $q_y$ , needed for instability of the zonal flow. Negative regions of quasi-geostrophic potential vorticity gradient are shaded in Fig. 2d. The three negative regions associated with the inner vortex change with time as the fast inner vortex interacts with the slower changing main vortex. Though this paper focuses on the waves interacting with a zonally averaged basic state, the complicated negative  $q_y$  pattern, with its lack of zonal symmetry, should be kept in mind. In addition to wave 2, the patterns in Fig. 2 show a wave 1 component as well, in that the disturbance is centered somewhat off the pole: however, the wave 2 feature stands out more clearly at this time.

A representative 6 month time series (April–September 1998) of temperature and ozone at a point at 70°S and 2 hPa (Fig. 3) shows 2–4 day fluctuations throughout the time period. The temperature and ozone oscillations increase in amplitude during July 1998, though the ozone shows larger amplitudes than temperature in May and June. There is some visual evidence here (verified by spectral analysis) that the period of the oscillations is higher in July than in August. This corresponds to dominance of wave 2 over wave 1 in July.

Fig. 4 shows the zonal average temperature and ozone at 2 hPa as a function of time

and latitude. While the ozone gradients increase somewhat with time, the temperature structure changes dramatically in July 1998, with a relatively warm region forming at 60-70°S and increased meridional temperature gradients poleward of 70°S. As will be shown, this warm region is where the wave 2 component of the 4-day wave is found.

Fig. 5 shows the July 1998 eastward propagating temperature and ozone frequency spectrum as a function of pressure at 70°S for wave 1 and wave 2. Also plotted is the critical line, derived from the zonal mean zonal wind, for each frequency and wavenumber. Note that most wave activity is bounded by the critical line indicating that the waves are regressing with respect to the zonal mean winds as expected for Rossby waves. The wave 1 temperature spectra (Fig. 5a) are large for the stationary and slowly propagating waves, however the amplitudes are relatively weak and poorly defined near the 4-day wave frequency ( $0.25 \text{ day}^{-1}$ ). The wave 1 ozone spectra (Fig. 5b) show a stationary wave peak at 2 hPa and a weak ozone peak at a fairly high period ( $0.4 \text{ day}^{-1}$ ) very near the critical level. The wave 2 temperature spectra (Fig. 5c) show a large, vertically coherent peak at about  $0.6 \text{ day}^{-1}$ . This is the wave 2 structure: the period is about 1.7 days. The spectral peak maximizes between 1-2 hPa and extends from the top of the domain down to the critical level. The wave 2 ozone spectra (Fig. 5d) shows a similar  $0.6 \text{ day}^{-1}$  peak, though it is much more localized in the vertical than the wave 2 temperature peak. Ozone also tends to show a weak peak

at higher frequencies near the critical level, similar to the wave 1 ozone spectra.

The same frequencies as a function of latitude, at 2 hPa, are shown in Fig. 6. Once again the waves are generally constrained by the critical line to be propagating more slowly than the zonal mean flow. An exception seen here is near the equator where the peaks in the temperature spectra are likely to be Kelvin waves. The wave 1 temperature spectra (Fig. 6a) show the largest amplitudes at low frequencies (periods greater than 10 days). Poleward of 70°S there is a weak peak at  $0.25 \text{ day}^{-1}$ . The wave 1 ozone spectra (Fig. 6b) show low frequency waves along with high frequency peaks poleward of 70°S. As in Fig. 5, the ozone tends to show peaks near the critical level and peaks at even higher frequencies than the critical level frequency. The wave 2 temperature spectra (Fig. 6c) show low frequency waves equatorward of 60°S and the high frequency peak, as before, at  $0.6 \text{ day}^{-1}$ . The wave 2 ozone spectra (Fig. 6d) also show the  $0.6 \text{ day}^{-1}$  peak, along with peaks at higher frequencies near the critical level. The tendency seen here for the ozone frequencies to peak near the critical level may represent advection of ozone features by the zonal mean wind and is discussed further in Section 5. Fig. 6 shows that the high frequency wave is larger and more well defined in wave 2 than wave 1 during July 1998 in agreement with Fig. 5.

As pointed out by Allen et al. (1997) and others, the 4-day wave temperature structure is expected to be a vertical dipole centered about a geopotential height (or pv)

perturbation. The two lobes of the temperature dipole will be out of phase with each other so that high perturbation heights will have warm air below and cold air above, consistent with hydrostatic balance. In this study, only the lower lobe of the temperature dipole can be seen, as the DAO pressure level output stops at 0.2 hPa. However, the geopotential height and pv waves can be examined above the lower temperature lobe.

Figure 7 shows the wave 1 and wave 2 pv and geopotential height spectra for July 1998 at 0.4 hPa as a function of latitude. The pv and height spectra are similar. The wave 1 spectra (Figs. 7a and b) show the largest peaks for the low frequency waves with smaller peaks poleward of  $70^{\circ}\text{S}$  at  $0.25 \text{ day}^{-1}$  and higher frequencies. The wave 2 spectra (Figs. 7c and d) show some low frequency waves equatorward of  $60^{\circ}\text{S}$  and a well-defined high frequency peak at  $0.6 \text{ day}^{-1}$ . This wave 2 peak occurs near the intersection of the critical line and the latitude where  $\bar{q}_y = 0$ . This agrees with expectations from the linear theory of barotropically growing waves (as discussed in Hartmann 1983). Because of the double-peaked jet at these altitudes, the wave 2 frequencies from  $0.55\text{--}0.6 \text{ day}^{-1}$  actually have three critical lines (as can be seen in Fig. 7), and the two most poleward critical lines are close to the two  $\bar{q}_y = 0$  lines that bound the negative  $\bar{q}_y$  region between the two jets. Thus, the monthly averaged zonal mean zonal wind in July 1998 provides ample opportunity for the development of wave 2,  $0.55\text{--}0.6 \text{ day}^{-1}$

modes. What is not clear is why wave 2 is singled out for development rather than the corresponding wave 1 frequencies.

The next three plots (Figs. 8, 9, and 10) present a series of latitude-pressure sections of the July 1998 wave 2 structure at a single frequency,  $0.58 \text{ day}^{-1}$  (1.72 day period), that corresponds to the main wave 2 peak seen in the spectra. The critical line for this frequency is repeated on all the plots as a reference curve. Note that these plots are more limited in altitude (100–0.2 hPa) and latitude (90–30°S) than previous plots to better focus on the region of interest.

Figure 8a shows the zonal mean zonal wind for the month of July 1998 and its associated negative region of  $\bar{q}_y$ . The jet tilts strongly equatorward with altitude with a weak poleward secondary maximum at the uppermost levels. In between the two jets is the negative  $\bar{q}_y$  region. The critical line for the  $0.58 \text{ day}^{-1}$  wave and the  $\bar{q}_y = 0$  line coincide at upper levels, in the region between the two jets. The reference level at 0.4 hPa shows how there can be three critical levels at a given altitude as seen in Fig. 7. Figure 8b shows the zonal mean temperatures for July 1998. The dashed line shows where the meridional temperature gradient is zero. A region of reversed temperature gradient (warm air toward the pole) extends from the mesosphere down into the stratosphere.

Figure 8c shows the wave 2 temperature amplitude and phase. As mentioned above,

only the lower lobe of the temperature structure is seen at these altitudes, though the phase is changing rapidly with height at the top level, as expected, and there is some hint of an increase in amplitude beginning at 0.2 hPa. The temperature wave maximum (about 2.5 K) occurs right where the mean temperature gradients are reversed (Fig. 8b). The ozone amplitude maximum (Fig. 8d) is more poleward and lower down than the corresponding maximum in temperature amplitude. The ozone amplitude (maximum about 0.2 ppmv) is more confined in the vertical than the temperature amplitude and the ozone phase emphasizes the change in phase with latitude.

Figure 9a shows the wave 2 geopotential height field for July 1998. The maximum height amplitude (about 80 m) is near the critical line. The phase structure will be discussed below along with the EP (Eliassen-Palm) flux. Using output from a data assimilation system allows for examination of quantities not normally seen, such as vertical velocity (Fig. 9b). The vertical velocity perturbation is seen to peak (at about  $0.8 \times 10^{-2} \text{ m s}^{-1}$ ) in the negative  $\bar{q}_y$  region at the highest levels examined.

Figure 9c superimposes the ozone amplitude on top of a plot of the meridional gradient of the zonal mean ozone. The ozone wave amplitude peaks where the geopotential height amplitude (Fig. 9a) overlaps the peak in horizontal ozone gradient. Since the amplitude of the meridional wind perturbation associated with the wave (not shown) is well correlated with the amplitude of the geopotential perturbation (through geostrophic

balance) this implies that horizontal advection by the wave acting in a region of strong latitudinal ozone gradients is mainly responsible for the ozone wave signal, in agreement with the findings of Manney et al. (1998).

Figure 9d shows that temperature is not the only quantity with a dipole structure. The zonal mean wind perturbation shows a strong dipole structure in latitude associated with the height perturbation. A phase switch occurs between the two lobes. This structure is expected from geostrophic balance with the perturbation height field. The most equatorward lobe peaks at  $\sim 50^\circ\text{S}$ .

Figure 10a plots the EP flux divergence and the EP flux vectors calculated from the assimilated winds and temperatures for July 1998 wave 2 height field. The divergence is centered at about 1 hPa and  $58^\circ\text{S}$  with extensions up into the negative  $\bar{q}_y$  region and across over a broad latitude range ( $70\text{--}50^\circ\text{S}$ ) at 2 hPa. The EP flux vectors point into three convergence regions: equatorward (and above), poleward (and above) and below the divergence region. Linear instability theory predicts growing waves to consist of a dipole of EP flux divergence and convergence with the EP flux vector pointing from divergence to convergence (see Hartmann (1983) for a discussion of the barotropic problem and Manney and Randel (1993) for baroclinic examples). The July 1998 wave 2 shows a more complex case than what is usually modeled. The poleward and equatorward EP flux vectors show that both poleward and equatorward momentum fluxes are

associated with the wave. This helps explain the geopotential height field phase variations shown in Fig. 9a at upper levels where the meridional phase gradient changes sign. Downward EP flux vectors have been reported by Randel and Lait (1991) and Allen et al. (1997) and in the linear instability model of Manney and Randel (1993). These downward EP flux vectors are not surprising in a middle atmosphere instability event: however, they contrast with the usually upward direction associated with planetary waves propagating upward from the troposphere. The net EP flux will still be upward, of course, as the forced upward planetary fluxes are much larger than the fluxes associated with the local instability. These downward EP flux vectors penetrate to below 10 hPa where they abate near the lower part of the critical level.

Figure 10b shows the same fields as in Fig. 10a, but calculated using only the assimilated geopotential height field amplitude and phase shown in Fig. 9a, using the quasi-geostrophic approximation. Though the magnitudes are larger, the quasi-geostrophic approximation shows remarkable agreement with the full calculation. This lends support to observational EP-flux studies based only on satellite derived height fields.

Figure 10c plots the heat flux-based mass stream function (meridional heat flux divided by the mean stability) associated with the  $0.58 \text{ day}^{-1}$  wave 2. The circulation is equatorward at 2 hPa, opposite to the poleward motion forced by upward propagating planetary waves. The total circulation will be dominated by the upward propagating

planetary waves, however, the higher frequency wave signal can be seen as a perturbation in the over-all downward poleward motion (not shown).

The EP flux divergence is re-plotted (Fig. 10d) with a density scaling to better quantify the induced mean wind tendency. Most of the tendency occurs at the lowest density level shown, with the EP flux divergence acting to accelerate the wind in the region between the two jets and with the EP-flux convergence acting to decelerate the jet winds, especially the poleward jet. The maximum deceleration shown is about  $4 \text{ m s}^{-1} \text{ day}^{-1}$ .

The time behavior during July 1998 is examined by first putting the assimilation fields through a simple band pass filter that retains only eastward propagating wave 2 frequencies between  $0.4\text{--}1.0 \text{ day}^{-1}$ . Figure 11a shows the EP flux divergence at 2 hPa as a function of latitude and time based on the filtered assimilation products. The EP flux divergence shows how the wave forcing changes over the course of the month. The peak EP flux divergence location varies from about  $55^\circ\text{S}$  early in the month to  $\sim 60\text{--}70^\circ\text{S}$  later in the month. The largest values of EP flux divergence start on 13 July 1998 and consist of six peak events (13, 16, 18, 22, 25, and 28 July). Figure 11b shows the time evolution of the zonal mean zonal wind along with the  $0.58 \text{ day}^{-1}$  critical level and the negative  $\bar{q}_y$  regions, all at 2 hPa. The three later EP flux divergence peaks (22, 25, and 28 July) are seen to occur about a half a

day after the center of corresponding negative  $\bar{q}_y$  regions. There is also some overlap between the EP flux divergence on 9 July and a negative  $\bar{q}_y$  region.

Figure 12 shows the same fields as Fig. 11 at 0.4 hPa. The zonal mean zonal wind (Fig. 12b) shows the double jet structure at these altitudes with a persistent region of negative  $\bar{q}_y$  located between the two jets. Unlike the nearly constant single critical line at 2 hPa, at 0.4 hPa there are often times when the  $0.58 \text{ day}^{-1}$  critical line is found at three latitudes. Note how the  $0.58 \text{ day}^{-1}$  critical line mirrors the poleward most  $\bar{q}_y = 0$  line during most of the time shown and tracks closely the middle critical line about half of the time shown. The EP flux divergence at 0.4 hPa is mainly in the negative  $\bar{q}_y$  region with EP flux convergence outside the negative  $\bar{q}_y$  region as expected from linear stability arguments for growing waves. This relation is especially apparent on 14 July.

Figure 13 shows the EP flux divergence and the zonal mean zonal wind at 4 times: 7 Jul 6 UTC; 13 Jul 18 UTC; 18 Jul 0 UTC; and 22 Jul 6 UTC. Because these fields are not time averages and contain a range of frequencies, the magnitude of the EP flux vectors and their divergences are larger than in the monthly averaged, single frequency plots previously shown in Fig. 10 and the vectors and contours have been re-scaled for these plots. Early in the month (Fig. 13a) the EP flux divergence is relatively weak and located at a relatively low latitude ( $55^\circ\text{S}$ ). There are two EP flux convergence regions both poleward and equatorward of the peak divergence region, with EP flux vectors

pointing from the divergence region into the convergence regions. These vectors correspond to both equatorward and poleward momentum fluxes at this time. This pattern of EP flux divergence will tend to accelerate the winds between the split jet (Fig. 13b) and decelerate both jets. The EP flux divergence at this time is somewhat correlated with the negative  $\bar{q}_y$  region located between the split jet.

By 13 July, the EP flux divergence (Fig. 13c) is much stronger and the peaks are displaced farther poleward ( $65^\circ\text{S}$ ). While the EP flux divergence peaks below the negative  $\bar{q}_y$  region, there is still an EP flux divergence region above 1 hPa that is well correlated with the negative  $\bar{q}_y$  region. There are two EP flux convergence regions at this time: one above and poleward of the main divergence peak, and one below the EP flux divergence region. The EP flux vectors are mainly poleward at this time (equatorward momentum fluxes) except down near 10 hPa where the EP flux vectors head toward the critical level (Fig. 13d).

An even more poleward EP flux divergence peak is found on 18 July (Fig. 13e) and it is clearly associated with a high latitude negative  $\bar{q}_y$  region. The poleward jet is very weak at this time (Fig. 13f) and most of the EP flux vectors equatorward of  $70^\circ\text{S}$  point equatorward (poleward momentum flux). The EP flux convergence region completely encircles the divergence region with especially strong convergence above and below the divergence region.

Just 4 days later (about one rotational period) the EP flux divergence peak (Fig. 13g) is more equatorward ( $58^{\circ}\text{S}$ ) and there are large regions of both poleward and equatorward EP flux vectors. The EP flux divergence is well correlated with a negative  $\bar{q}_y$  region and the double jet structure has returned (Fig. 13h). The EP flux convergence region wraps almost completely around the divergence region.

#### **4 POAM Ozone Data**

This section presents POAM (Polar Ozone and Aerosol Measurement) ozone data (Lucke et al. 1999) that observationally validates key features of the 4-day wave as seen in the DAO ozone assimilation. During July 1998 the POAM ozone observations were confined between about  $65\text{--}70^{\circ}\text{S}$  and therefore will be treated as being at a constant latitude. There are  $\sim 14$  ozone profiles taken each day. This does not give much resolution for a longitude time plot: nevertheless, Fig. 14 shows one attempt to interpolate the longitude-time POAM observations at 2 hPa to a regular grid suitable for contouring the high frequency waves. Comparing with the assimilation ozone (Fig. 1b), the POAM observations show a similar time mean wave 1 structure and propagating wave 2 feature. The amplitude of the wave 2 signal in the POAM ozone is nearly the same as in the DAO ozone assimilation (the contour interval is doubled in Fig. 14), although there

is an offset to slightly higher overall values of ozone in the POAM observations.

Figure 15 provides more quantitative evidence of the high frequency wave in the POAM observations using an analysis method similar to that of Prata (1984). Here the POAM observations at each level are taken as a time series for the month and a Fourier transform is performed on the month long time series (431 points at each level for the month of July 1998). This method does not separate out the wavenumber dependence, however stationary waves 1 and 2 would correspond to  $1 \text{ day}^{-1}$  and  $2 \text{ day}^{-1}$  frequencies respectively (as the Earth rotates under the satellite), and 4 day rotational period, westward propagating waves 1 and 2 would correspond to  $1.25 \text{ day}^{-1}$  and  $2.5 \text{ day}^{-1}$  frequencies respectively (by adding the frequency of the wave motion to the corresponding frequency associated with the Earth's rotation). The results are plotted in two frequency ranges (Fig. 15a and b) to aid in making comparisons with Fig. 5b and d. Figures 15a and 15b can be interpreted as wave 1 and wave 2 plots, though this interpretation of the POAM observations is not unique.

Spectral analysis of the POAM time series confirms what can easily be seen as the largest signal in the time series: an oscillation near 2 hPa with a frequency of  $2.58 \text{ days}^{-1}$  (Fig 15b). A stationary wave 2 would yield a peak of  $2 \text{ days}^{-1}$  and an eastward propagating wave 2 would have  $2 \text{ days}^{-1}$  added to its frequency, in this case  $0.58 \text{ days}^{-1}$ , exactly the peak seen in the DAO ozone assimilation and temperature

(Fig. 5). Of course, the peak at  $2.58 \text{ days}^{-1}$  could also be produced by a very rapidly moving eastward wave 1 or a westward propagating wave 3. However, the wave 2 interpretation seems most likely in this case, given the DAO assimilation results. Only a portion of the POAM spectrum is shown in Fig. 15: however, the  $2.58 \text{ day}^{-1}$  frequency peak is by far the largest spectral peak. The magnitude of the  $2.58 \text{ day}^{-1}$  peak is about the same as that found in the DAO ozone spectra (fig. 5d) and the peak is located at  $\sim 2 \text{ hPa}$  in both the POAM ozone spectra and the DAO ozone spectra.

Figure 15a shows a stationary wave 1 signal (also apparent in Fig. 14) at  $1 \text{ day}^{-1}$  and a very small peak at  $1.4 \text{ day}^{-1}$  that can be interpreted as corresponding to the small wave 1 ozone peak seen in Fig. 5b at  $0.4 \text{ day}^{-1}$ . As pointed out in the discussion of Fig. 5b, this peak is near the frequency corresponding to the mean wind speed (i.e. near the critical line).

## 5 Discussion

The assimilation products shown here clearly display high frequency planetary-scale waves over the pole during the southern hemisphere winter. Issues to be discussed concern the quality of the assimilation products for high frequency wave studies, the ability of linear instability theory to explain the results, and the advective peaks seen in

the ozone spectra.

*a. Quality*

The meteorological data going into the fvDAS at these levels (2 hPa) are mainly satellite radiance measurements. That these observations contain the 4-day wave is not surprising given that the early work in studying the 4-day wave (Venne and Stanford 1979, 1982; Prata 1984) was based directly on satellite radiances. The fvDAS used a 1DVAR assimilation (Joiner and Rokke 2000) of satellite radiances and should reflect any waves in these radiances. However a good representation of the waves is needed in the GCM as well in order for them to persist in the analysis. The ability of the fvGCM to realistically represent these wave has not been studied to date.

The top level of the analysis may be too low to completely characterize the waves. As mentioned in the introduction, the top analysis level is 0.4 hPa with the highest pressure level output being slightly above it at 0.2 hPa. The negative  $\bar{q}_v$  region and the wave 2 critical level extend above this altitude. It would be more satisfying if the entire regions of unstable and high zonal wind speeds were captured. The fvGCM does extend to 0.01 hPa so the whole region of instability may indeed be contained by the fvDAS.

The ozone data assimilation system was run without chemistry at this time, relying on observations to correct for photochemical modifications. This may lead to some biases in the mean values and wave amplitudes in the ozone assimilation, however, the basic patterns should be captured via advection by the fvGCM coupled with the ozone observations, since past studies have shown the 4-day wave signal in ozone (Allen et al. 1997) and other tracer gases (Manney et al. 1998) is predominantly a transport phenomenon. Here, the 4-day wave signal in the DAO assimilated ozone agreed well with contemporaneous POAM ozone observations.

Band-passed filtered fields were used here because the 2-day wave signal was well-defined and persistent throughout July 1998. Generally the band passed filtered fields closely followed the full wave pattern (by comparison of corresponding maps, not shown): however, there were some specific times (mainly at the end of the month) when the band-passed filtered temperatures did not closely resemble the warm temperature regions. At these times enhanced wave 1 and wave 3 components were also present, and thus, more spectral components or a non Fourier approach are required taken for detailed study of the dynamical situation at these times.

The key to this study was the availability of fvDAS products every 6 hours. Such time resolution resolves these fast propagating and fast changing waves and thus permits a detailed study of their properties and evolution.

*b. Instability theory*

In linear instability theory a negative  $\bar{q}_y$  region is correlated with a region of EP flux divergence. Hartmann (1983) found exact correlation in his barotropic model. In their baroclinic model Manney and Randel (1993) also found EP flux divergence and negative  $\bar{q}_y$  regions were very closely correlated. In this study, we found that regions of EP flux divergence were not so well correlated with negative  $\bar{q}_y$  regions. Throughout the month of July 1998, the EP flux divergences are closely associated with a negative  $\bar{q}_y$  region, however, the negative  $\bar{q}_y$  regions seem to disappear quickly once a region of EP flux divergence appears. The negative  $\bar{q}_y$  region is never completely eliminated, but rather tends to shift to a different latitude or height.

Some of the wave structure seems to show wave propagation away from the source region toward convergence at a critical level. This can be seen in Fig. 10a where the EP flux vectors converge on the critical line at about 20 hPa. By contrast, EP flux vectors from a linear model shown in Manney and Randel (1993) are only large close to the negative  $\bar{q}_y$  region.

Fig. 2d shows how zonally asymmetric the negative potential vorticity regions can be. This suggests that (in this example at least) formulating the problem in terms of waves growing on a zonally symmetric unstable state may only be a first step in un-

derstanding the origin and evolution of the waves. All of the zonally averaged EP flux divergence regions shown here overlap with negative potential vorticity regions at some longitude (not shown). Additional consideration of wave-wave interactions (Manney et al. 1989) or a more three-dimensional modelling approach may be needed.

Overall, our study supports earlier linear instability models that associate regions of potential vorticity instability as the source of the waves. The waves propagate (where  $\bar{q}_y$  is positive) more slowly than the mean wind in agreement with Rossby wave theory. In addition the wave's vertical scale decreases as the waves approach the critical level from above, as seen in Fig. 9a where the phase of the geopotential height field begins to change rapidly, again in agreement with linear Rossby wave theory. The frequency of the wave is determined by the near coincidence of the  $\bar{q}_y = 0$  line and a constant zonal mean zonal wind line (critical line) in the region between the double jet.

*c. Advective ozone peak*

While the temperature spectra peak at frequencies that imply phase speeds slower than the zonal mean zonal wind, the ozone spectra show a tendency for additional peaks at frequencies that imply phase speeds that are faster than the zonal mean zonal wind speed (Fig. 6). This may imply that the wave-induced temperature response is more

dynamically controlled than the ozone response. Chemistry or diabatic processes may act to create ozone gradients along pv contours allowing the wave-induced ozone response to have a passive advection signal as well. While no signals like this were seen in Manney et al. (1998) a large fast moving ozone peak was seen in the spectra presented in Allen et al. (1997). The results here should be interpreted with some caution as these advective peaks were not identified prior to the spectral analysis and the relation between the spectra of advected tracers to the zonal mean zonal wind speed has not been investigated explicitly here.

As recognized by past studies (Prata 1984; Lawrence et al. 1995), the wave temperature perturbation is not simply being advected by the zonal mean zonal wind. Indeed, our results show that the temperature perturbations are generally moving more slowly than the mean wind. The DAO ozone assimilation results serve as a reminder that advection is more likely to produce filaments, rather than well-defined isolated temperature regions. This can be seen to some extent in Fig. 2, where the temperature map has less filamentary structure than the corresponding ozone map.

## 6 Conclusion

This paper has focused on a month (July 1998) when the wave 2 component of the 4-day wave was well defined and persistent. The availability of 6 hourly output from the fvDAS has allowed the first detailed global examination of this fast moving wave feature. In addition, a companion ozone assimilation allowed identification of the high frequency wave in the assimilated ozone field.

This wave 2 component (1.7 day period) is generally consistent with past observational studies and linear instability models. Enhanced EP flux divergence is closely associated with negative  $\bar{q}_y$  regions with the wave amplitude mainly confined by the critical line to phase speeds westward with respect to the mean flow..

The wave 2 also appears prominently in the DAO ozone assimilation, having an amplitude of about 0.5 ppmv or  $\sim 15\%$  of the total ozone mixing ratio at 2 hPa. This ozone signal is supported by independent POAM ozone mixing ratio observations. POAM ozone time series at  $\sim 70^\circ\text{S}$  shows a spectral peak at  $2.58 \text{ day}^{-1}$  that is consistent with the assimilation results. The amplitude of the  $2.58 \text{ day}^{-1}$  signal in POAM (Fig. 14) is very close to the amplitude of the wave 2,  $0.58 \text{ day}^{-1}$  signal in the DAO ozone assimilation (Fig. 5d) and both show the ozone spectra at those frequencies peaking near 2 hpa.

In addition to the 4-day wave peaks, the ozone assimilation showed high frequency peaks corresponding to advection with the zonal mean zonal wind speed. These peaks may be related to mean advection of chemically or diabatically-induced ozone gradients along the pv contours.

While the wave can appear fairly steady over the course of a month, the EP flux divergence pattern can vary significantly over the course of a wave period as shown here for the wave 2 component and in Randel and Lait (1991) and Lawrence and Randel (1996) for the wave 1 component. This probably indicates that more detailed examination of these wave and their development may be possible using instantaneous pv maps. This leaves open future studies based on assimilation products to further understand the origin and development of high frequency polar waves.

**Acknowledgment** We would like to thank Stephen Eckermann for reviewing an early draft of this work. We would also like to thank the POAM team for guidance in using the POAM ozone measurements. The work was supported in part by the Naval Research Laboratory.

## References

- Allen, D. R., J. L. Stanford, L. S. Elson, E. F. Fishbein, L. Froidevaux, and J. W. Waters, 1997: The 4-day wave as observed from the Upper Atmosphere Research Satellite Microwave Limb Sounder. *J. Atmos. Sci.*, **54**, 420–434.
- Andrews, D. G., J. R. Holton, and C. B. Leovy, 1987: *Middle Atmosphere Dynamics*. Academic Press, 489 pp.
- Cohn, S. E., A. da Silva, J. Guo, M. Sienkiewicz, and D. Lamich, 1998: Assessing the effects of data selection with the DAO physical-space statistical analysis system. *Mon. Weather. Rev.*, **126**, 2913–2926.
- Hartmann, D. L., 1983: Barotropic instability of the polar night jet stream. *J. Atmos. Sci.*, **40**, 817–835.
- Joiner, J. and L. Rokke, 2000: Variational cloud clearing with tovs data. *Quart. J. Roy. Meteor. Soc.*, **126**, 725–748.
- Lait, L. R. and J. L. Stanford, 1988: Fast, long-lived features in the polar stratosphere. *J. Atmos. Sci.*, **45**, 3800–3809.
- Lawrence, B. N., G. J. Fraser, R. A. Vincent, and A. Philips, 1995: The 4-day wave in the Antarctic mesosphere. *J. Geophys. Res.*, **100**, 18899–18908.

- Lawrence, B. N. and W. J. Randel, 1996: Variability in the mesosphere observed by the Nimbus 6 PMR. *J. Geophys. Res.*, **101**, 23475–23489.
- Lucke, R. L., D. R. Korwan, R. M. Bevilacqua, J. S. Hornstein, E. P. Shettle, D. T. Chen, M. Daehler, J. D. Lumpe, M. D. Fromm, D. Debrestian, B. Neff, M. Squire, G. König-Langlo, and J. Davies, 1999: The Polar Ozone and Aerosol Measurement (POAM) III instrument and early validation results. *J. Geophys. Res.*, **104**, 18785–18799.
- Manney, G. L., 1991: The stratospheric 4-day wave in NMC data. *J. Atmos. Sci.*, **48**, 1798–1811.
- Manney, G. L., T. R. Nathan, and J. L. Stanford, 1988: Barotropic stability of realistic stratospheric jets. *J. Atmos. Sci.*, **45**, 2545–2555.
- 1989: Barotropic instability of basic states with a realistic jet and a wave. *J. Atmos. Sci.*, **46**, 1250–1273.
- Manney, G. L., Y. J. Orsolini, H. C. Pumphrey, and A. E. Roche, 1998: The 4-day wave and transport of UARS tracers in the austral polar vortex. *J. Atmos. Sci.*, **55**, 3456–3470.

Manney, G. L. and W. J. Randel, 1993: Instability at the winter stratopause: A mechanism for the 4-day wave. *J. Atmos. Sci.*, **50**, 3928–3938.

Prata, A. J., 1984: The 4-day wave. *J. Atmos. Sci.*, **41**, 150–155.

Randel, W. J. and L. R. Lait, 1991: Dynamics of the 4-day wave in the Southern Hemisphere polar stratosphere. *J. Atmos. Sci.*, **48**, 2496–2508.

Venne, D. E. and J. L. Stanford, 1979: Observations of a 4-day temperature wave in the polar winter stratosphere. *J. Atmos. Sci.*, **36**, 2016–2019.

— 1982: An observational study of high-latitude stratospheric planetary waves in winter. *J. Atmos. Sci.*, **39**, 1026–1034.

Štajner, I., L. P. Riishojgaard, and R. B. Rood, 2001: The GEOS ozone data assimilation system: Specification of error statistics. *Q. J. R. Met. Soc.*, **127**, 1069–1094.

## List of Figures

- 1 Longitude time plot of (a) temperature (K) and (b) ozone mixing ratio (ppmv) at 70°S and 2 hPa for July 1998. Temperature contour interval is 5 K. Cooler temperatures are shaded. Ozone contour interval is 1 ppmv. Lower ozone values are shaded. . . . . 41
- 2 Circulation at 2 hPa on 16 July 1998 12Z: (a) temperature (K), temperatures less than 235 K shaded, contour interval 2.5 K; (b) potential vorticity (pvu, where  $1 \text{ pvu} = 1 \times 10^{-6} \text{ K m}^2 \text{ kg}^{-1} \text{ s}^{-1}$ ) pv less than -5500 pvu shaded, contour interval 500 pvu; (c) ozone (ppmv), ozone less than 2.5 ppmv shaded, contour interval 0.5 ppmv, and; (d) zonal wind component ( $\text{m s}^{-1}$ ),  $q_y$  less than zero is shaded, contour interval  $10 \text{ m s}^{-1}$ . Orthographic projection from equator to South Pole, 90° East at the bottom of the plots, highlighted latitude at 70° South. . . . 42
- 3 Time series of (a) temperature (K) and (b) ozone (ppmv) at 0° longitude, 70° south latitude. Time resolution is 6 hr. Altitude is 2 hPa. . . 43

- 4 Latitude-time contour plot of (a) temperature (K), 5 K contour interval, dark shading: temperatures less than 235 K, light shading: temperatures less than 245 K and (b) ozone (ppmv), 1 ppmv contour interval, shading: ozone less than 3.5 ppmv. Altitude is 2 hPa. . . . . 44
- 5 July 1998 wave amplitudes as a function of frequency (cycles day<sup>-1</sup>) and pressure at 70°S: (a) wave 1 temperature (K), (b) wave 1 ozone (ppmv), (c) wave 2 temperature (K), and (d) wave 2 ozone (ppmv). Temperature contour interval 0.5 K. Ozone contour interval 0.05 ppmv. The thicker solid curve plots the critical line at 70°S. The vertical dashed lines highlight the 4 day (for wave 1) and 2 day (for wave 2) frequencies. The horizontal dotted line is at 2 hPa. Values below 500 hPa are not shown. Larger amplitudes are shaded. . . . . 45

- 6 July 1998 wave amplitudes as a function of frequency (cycles day<sup>-1</sup>) and latitude at 2 hPa: (a) wave 1 temperature (K), (b) wave 1 ozone (ppmv), (c) wave 2 temperature (K), and (d) wave 2 ozone (ppmv). Temperature contour interval is 0.5 K. Ozone contour interval is 0.05 ppmv. The thicker solid curve plots the critical line at 2 hPa. The vertical dashed lines highlight the 4 day (for wave 1) and 2 day (for wave 2) frequencies. The horizontal dotted line is at 70°S. Larger amplitudes are shaded. . . . . 46
- 7 July 1998 wave amplitudes as a function of frequency (cycles day<sup>-1</sup>) and latitude at 0.4 hPa: (a) wave 1 potential vorticity (pvu), (b) wave 1 geopotential heights (m), (c) wave 2 potential vorticity (pvu), and (d) wave 2 geopotential heights (m). Potential vorticity contour interval 1000 pvu. Geopotential height contour interval 50 m. The thicker solid curve plots the critical level at 0.4 hPa. The diagonally striped region denotes latitudes where  $\bar{q}_v$  is negative. The vertical dashed lines highlight the 4 day (for wave 1) and 2 day (for wave 2) frequencies. The horizontal dotted line is at 70°S. Larger amplitudes are shaded. . . 47

8 Wave 2 structure, July 1998, 1.72 day period, as a function of latitude and pressure. The heavy dark curve is the critical line. (a) zonal mean zonal wind ( $\text{m s}^{-1}$ ). Shaded region is where the zonal mean pv gradient,  $\bar{q}_y$ , is negative. Dotted reference line at 0.4 hPa (b) zonal mean temperature (K). Thicker dashed curve is where the horizontal temperature gradient is zero. Shaded region is where  $\bar{q}_y$ , is negative. (c) temperature wave amplitude (K, shaded contours, contour interval 0.5 K) and phase (degrees, black lines, contour interval  $45^\circ$ ). (d) ozone wave amplitude (ppmv, shaded contours, contour interval 0.05 ppmv) and phase (degrees, black lines, contour interval  $45^\circ$ ). Reference broken lines at  $70^\circ\text{S}$  and 2 hPa in (c) and (d). . . . . 48

9 Wave 2 structure, July 1998, 1.72 day period, as a function of latitude and pressure. The heavy dark curve is the critical line. (a) geopotential height wave amplitude (m, shaded contours, contour interval 10 m, maximum contour is 80 m) and phase (degrees, black lines, contour interval 10°). Dotted reference line at 0.4 hPa; (b) vertical velocity amplitude ( $\times 10^{-2} \text{ m s}^{-1}$ , shaded contours, contour interval  $0.1 \times 10^{-2} \text{ m s}^{-1}$ ) and phase (degrees, black lines, contour interval 20°); (c) mean latitudinal ozone gradient ( $\text{ppmv deg}^{-1}$ , shaded contours, contour interval  $0.025 \text{ ppmv deg}^{-1}$ ) and ozone wave amplitude (dashed lines) taken from Fig. 8d; (d) zonal wind amplitude ( $\text{m s}^{-1}$ , shaded contours, contour interval  $1 \text{ m s}^{-1}$ ) and phase (degrees, black lines, contour interval 30°). . . . . 49

- 10 Wave 2 structure, July 1998, 1.72 day period, as a function of latitude and pressure. The heavy dark curve is the critical line. (a) EP flux divergence ( $10^{-2} \text{ kg m}^{-1} \text{ s}^{-2}$ ), negative values are shaded, contour interval  $10^{-2} \text{ kg m}^{-1} \text{ s}^{-2}$ , and arrows depict the EP flux vectors. (b) same as (a) except calculated from heights using quasi-geostrophic approximation. (c) wave-induced mass stream function ( $\times 10^5 \text{ kg s}^{-1}$ ), contours, negative values are shaded, contour interval  $10 \times 10^5 \text{ kg s}^{-1}$  and EP flux vectors from (a). (d) zonal mean wind forcing ( $\text{m s}^{-1} \text{ day}^{-1}$ , negative values are shaded, contour interval  $0.5 \text{ m s}^{-1} \text{ day}^{-1}$ ) and EP flux vectors from (a). . . . . 50
- 11 Time-latitude plots at 2 hPa for July 1998: (a) band pass filtered EP flux divergence ( $\times 10^{-2} \text{ kg m}^{-1} \text{ s}^{-2}$ ), contour interval  $5 \times 10^{-2} \text{ kg m}^{-1} \text{ s}^{-2}$ , negative values are shaded, negative  $\bar{q}_y$  regions double outlined. (b) zonal mean zonal wind ( $\text{m s}^{-1}$ ), contour interval  $5 \text{ m s}^{-1}$ , negative  $\bar{q}_y$  regions shaded. Thick gray line is the  $0.58 \text{ day}^{-1}$  critical line. The 4 horizontal lines correspond to the 4 times shown in Fig. 13. . . . . 51
- 12 As in Fig. 11 but for the 0.4 hPa level. . . . . 52

- 13 Plots of EP flux divergence (left, contour interval  $2.5 \times 10^{-2} \text{ kg m}^{-1} \text{ s}^{-2}$ , negative values are shaded) and zonal mean zonal wind (right, contour interval  $10 \text{ m s}^{-1}$ ) at four times during July 1998. EP flux vectors are scaled to be 40% smaller than in Fig. 10 to aid readability. The heavy line on the right is the critical line for a 1.72 day period wave 2 mode. Negative  $\bar{q}_y$  regions are shaded on the right and  $\bar{q}_y = 0$  are double lines on the left. . . . . 53
- 14 Longitude-time plot of POAM ozone (ppmv) at an average latitude of  $68^\circ\text{S}$  and 2 hPa for July 1998. Contour interval is 0.5 ppmv. Lower ozone values are shaded. . . . . 54
- 15 POAM ozone spectra (ppmv day) for July 1998 as a function of frequency and pressure: (a) for the frequency range  $1\text{--}2 \text{ day}^{-1}$ , (b) for the frequency range  $2\text{--}3 \text{ day}^{-1}$ . The contour interval is 0.05 ppmv. Higher values are shaded. The plot is split into two panels to aid in comparison with Fig. 5b and d, and corresponding reference lines are drawn. Only POAM observations above 14 hPa (heavy solid line) were analysed. . . . . 55

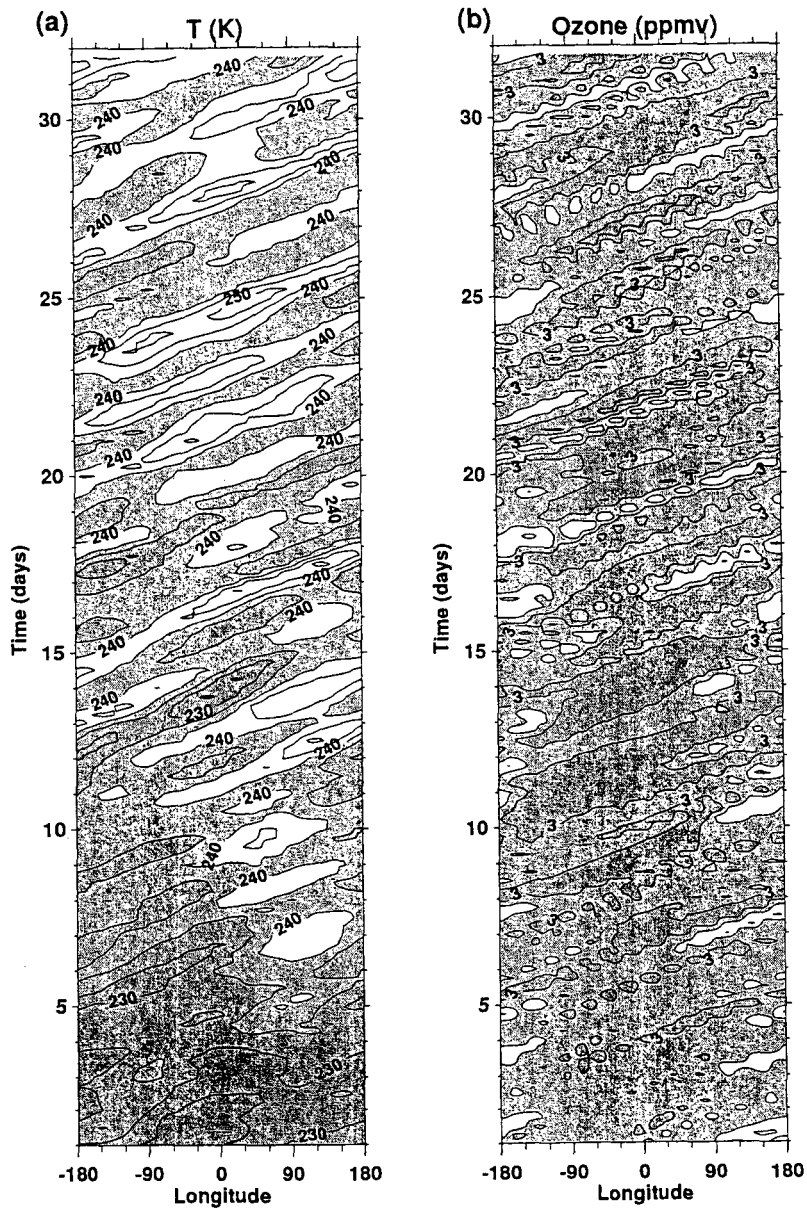


Figure 1: Longitude time plot of (a) temperature (K) and (b) ozone mixing ratio (ppmv) at 70°S and 2 hPa for July 1998. Temperature contour interval is 5 K. Cooler temperatures are shaded. Ozone contour interval is 1 ppmv. Lower ozone values are shaded.

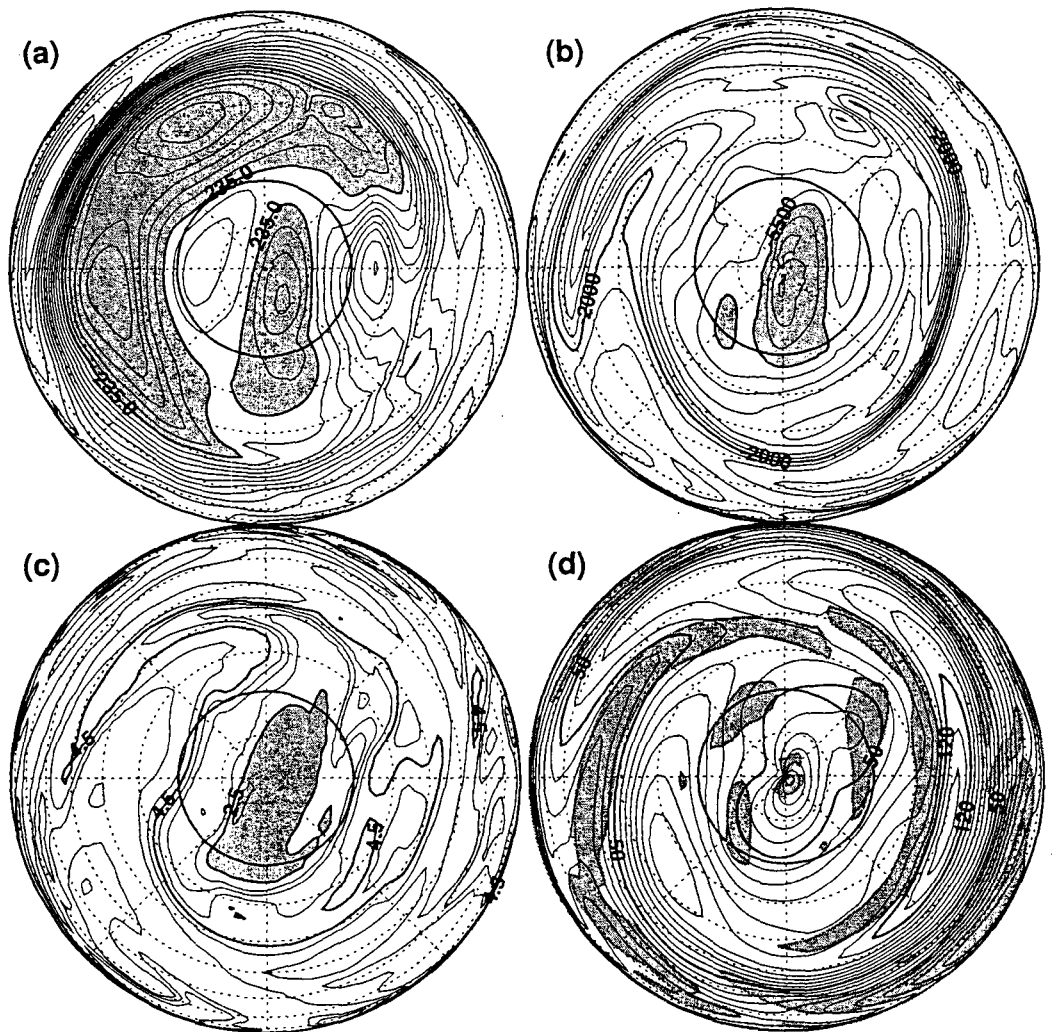


Figure 2: Circulation at 2 hPa on 16 July 1998 12Z: (a) temperature (K), temperatures less than 235 K shaded, contour interval 2.5 K; (b) potential vorticity (pvu, where  $1 \text{ pvu} = 1 \times 10^{-6} \text{ K m}^2 \text{ kg}^{-1} \text{ s}^{-1}$ ) pv less than  $-5500 \text{ pvu}$  shaded, contour interval 500 pvu; (c) ozone (ppmv), ozone less than 2.5 ppmv shaded, contour interval 0.5 ppmv, and; (d) zonal wind component ( $\text{m s}^{-1}$ ),  $q_y$  less than zero is shaded, contour interval  $10 \text{ m s}^{-1}$ . Orthographic projection from equator to South Pole,  $90^\circ$  East at the bottom of the plots, highlighted latitude at  $70^\circ$  South.

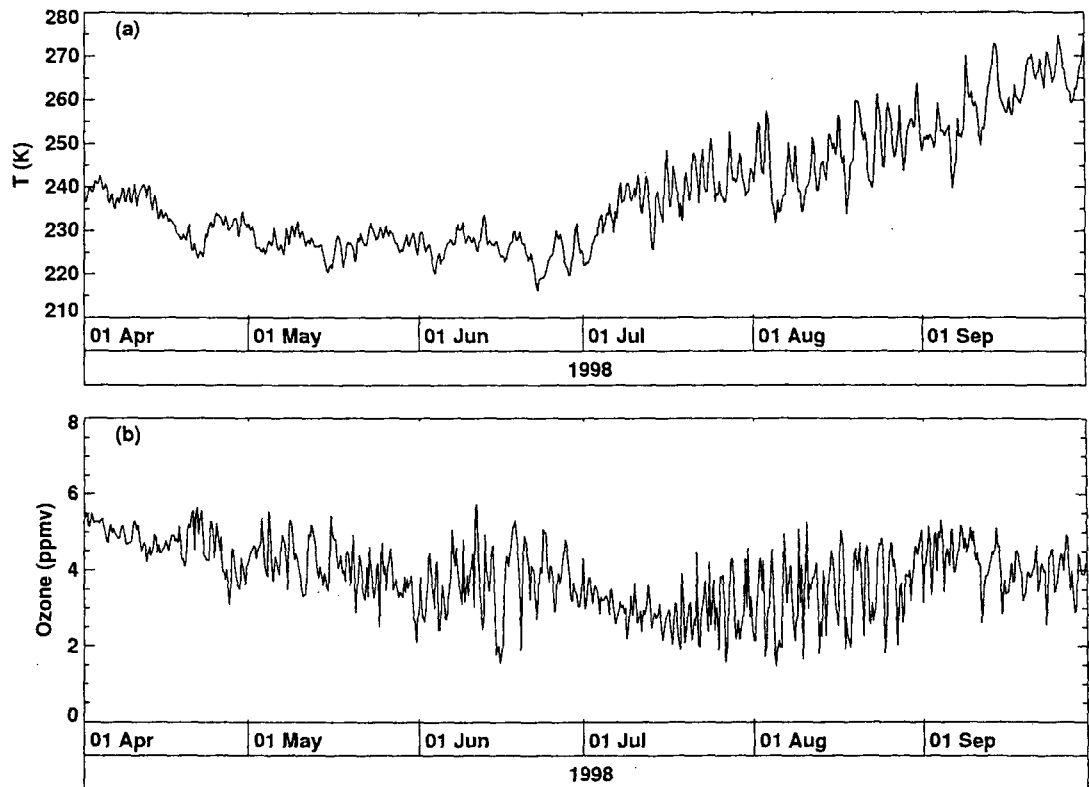


Figure 3: Time series of (a) temperature (K) and (b) ozone (ppmv) at  $0^\circ$  longitude,  $70^\circ$  south latitude. Time resolution is 6 hr. Altitude is 2 hPa.

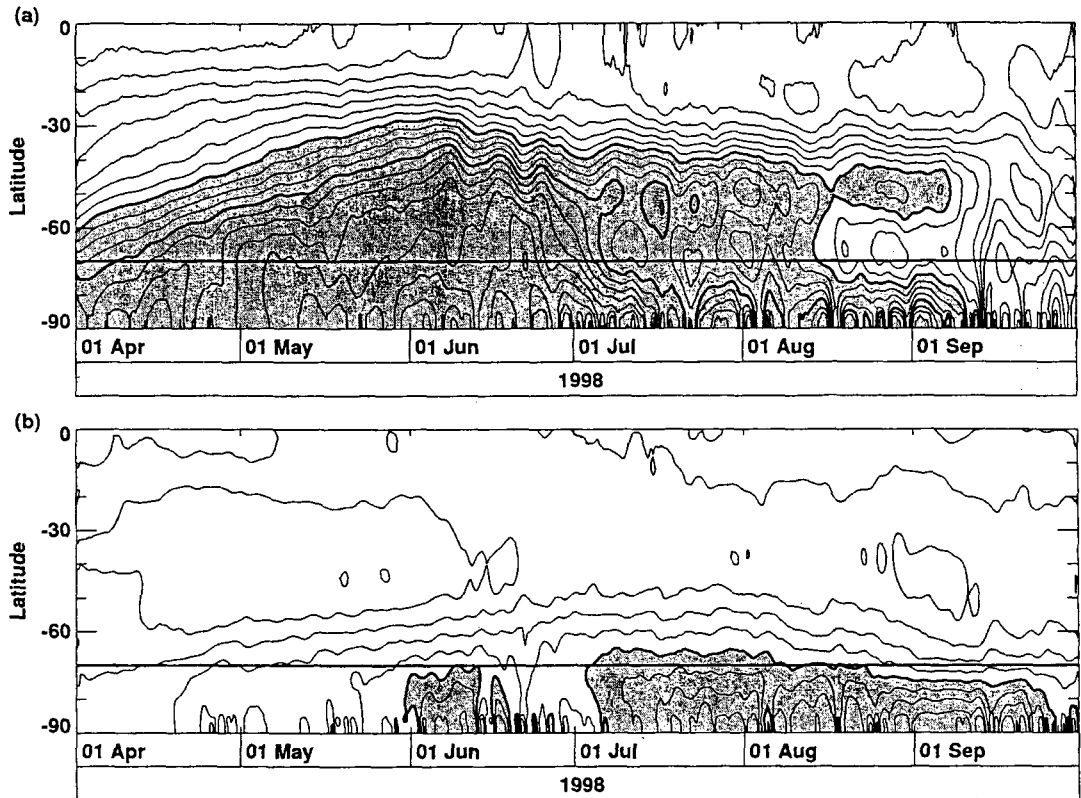


Figure 4: Latitude-time contour plot of (a) temperature (K), 5 K contour interval, dark shading: temperatures less than 235 K, light shading: temperatures less than 245 K and (b) ozone (ppmv), 1 ppmv contour interval, shading: ozone less than 3.5 ppmv. Altitude is 2 hPa.

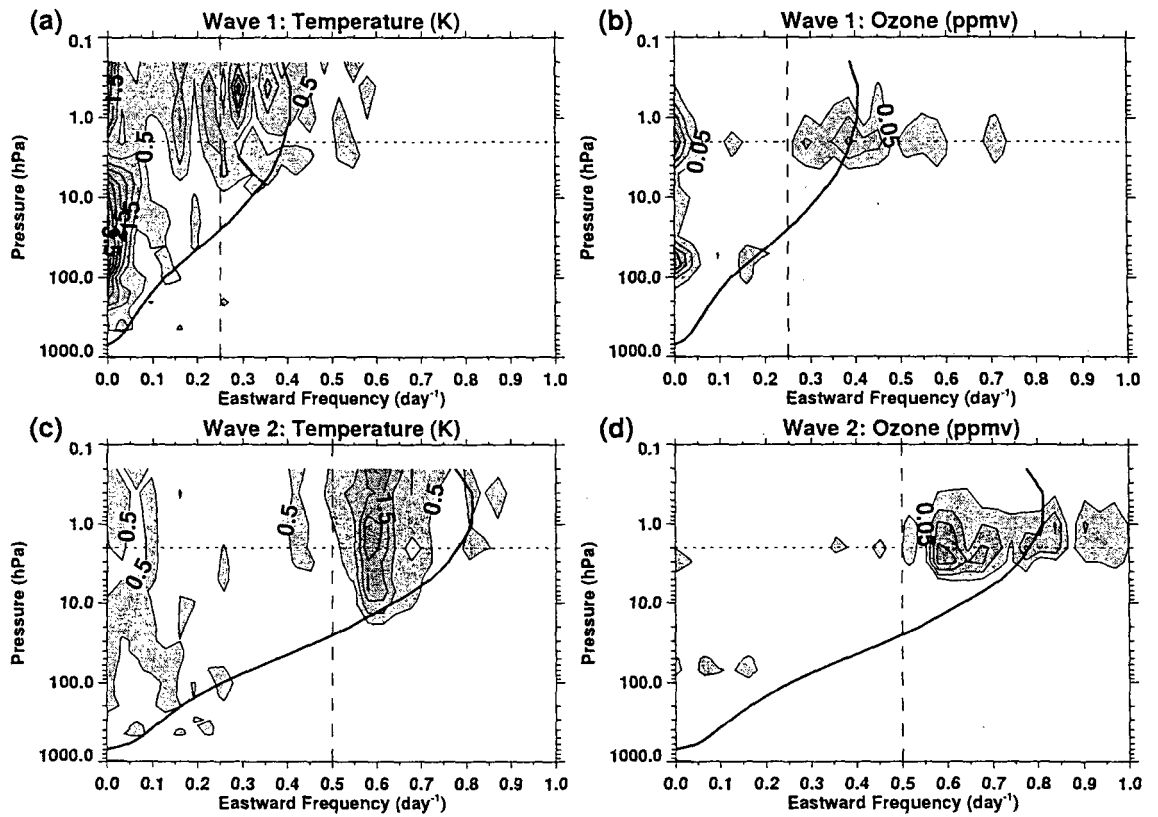


Figure 5: July 1998 wave amplitudes as a function of frequency (cycles day<sup>-1</sup>) and pressure at 70°S: (a) wave 1 temperature (K), (b) wave 1 ozone (ppmv), (c) wave 2 temperature (K), and (d) wave 2 ozone (ppmv). Temperature contour interval 0.5 K. Ozone contour interval 0.05 ppmv. The thicker solid curve plots the critical line at 70°S. The vertical dashed lines highlight the 4 day (for wave 1) and 2 day (for wave 2) frequencies. The horizontal dotted line is at 2 hPa. Values below 500 hPa are not shown. Larger amplitudes are shaded.

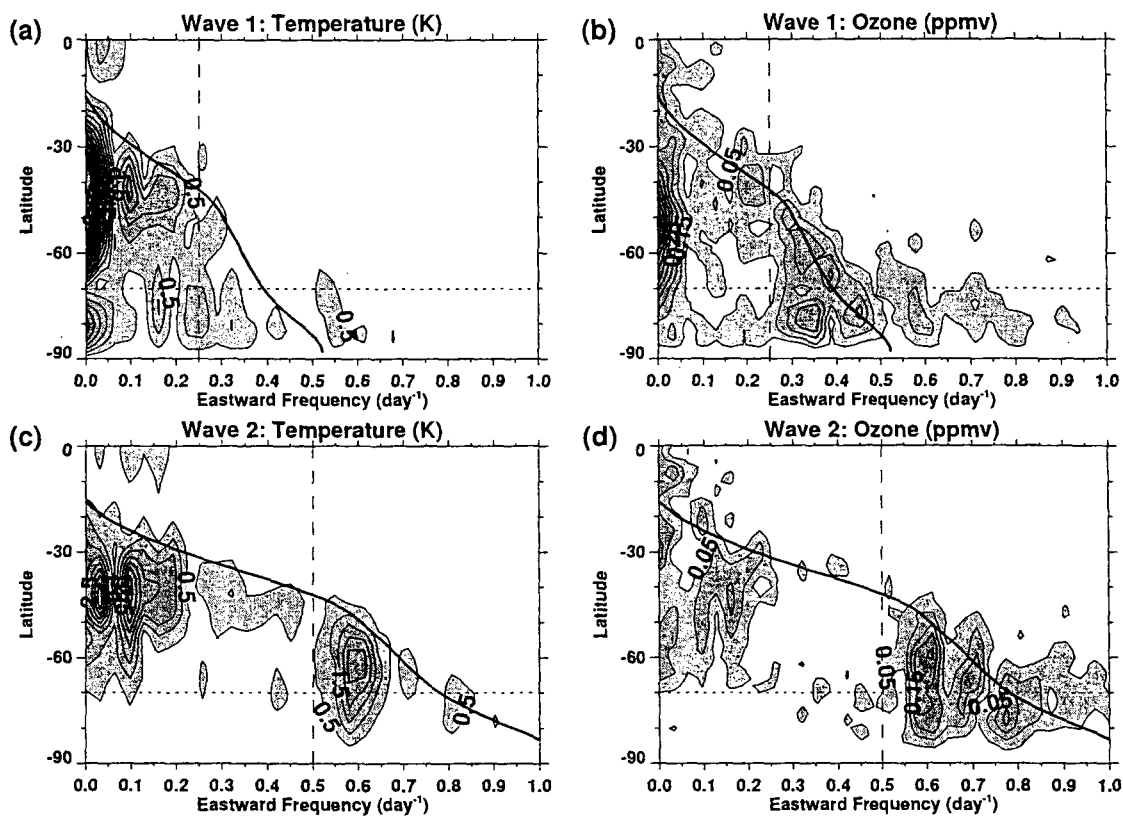


Figure 6: July 1998 wave amplitudes as a function of frequency (cycles day<sup>-1</sup>) and latitude at 2 hPa: (a) wave 1 temperature (K), (b) wave 1 ozone (ppmv), (c) wave 2 temperature (K), and (d) wave 2 ozone (ppmv). Temperature contour interval is 0.5 K. Ozone contour interval is 0.05 ppmv. The thicker solid curve plots the critical line at 2 hPa. The vertical dashed lines highlight the 4 day (for wave 1) and 2 day (for wave 2) frequencies. The horizontal dotted line is at 70°S. Larger amplitudes are shaded.

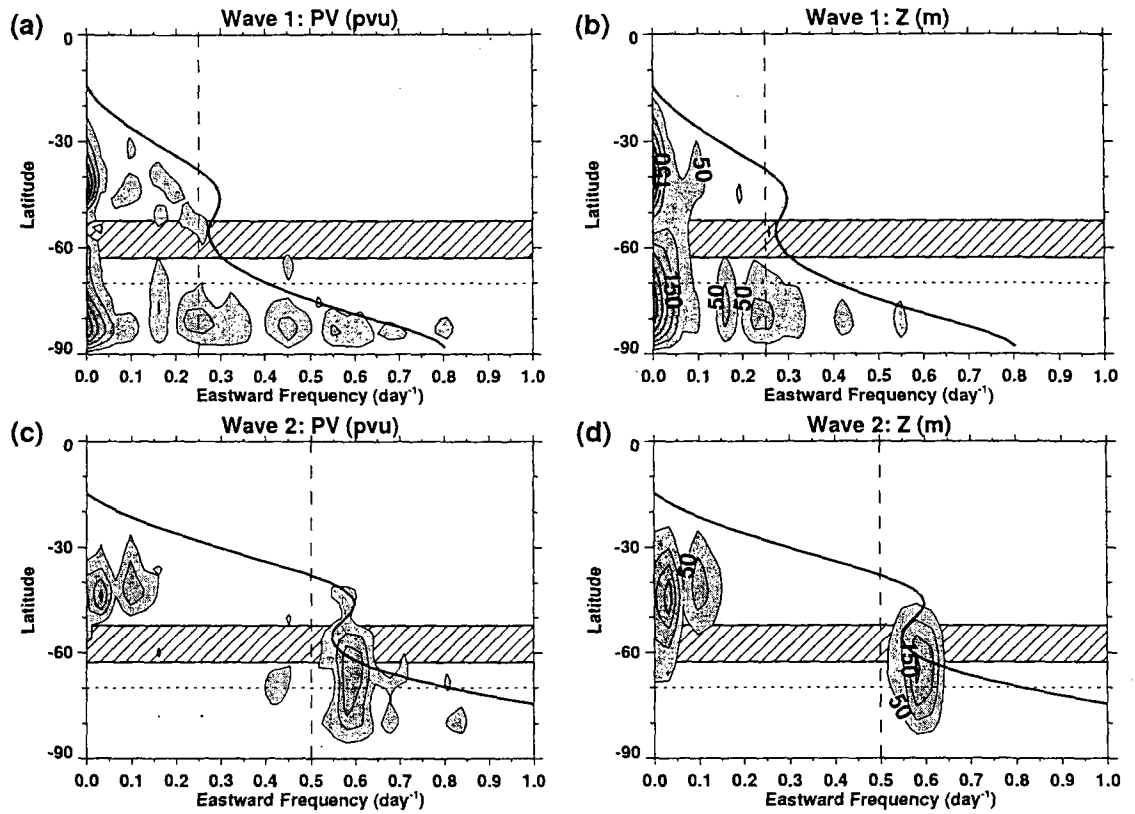


Figure 7: July 1998 wave amplitudes as a function of frequency (cycles  $\text{day}^{-1}$ ) and latitude at 0.4 hPa: (a) wave 1 potential vorticity (pvu), (b) wave 1 geopotential heights (m), (c) wave 2 potential vorticity (pvu), and (d) wave 2 geopotential heights (m). Potential vorticity contour interval 1000 pvu. Geopotential height contour interval 50 m. The thicker solid curve plots the critical level at 0.4 hPa. The diagonally striped region denotes latitudes where  $\bar{q}_y$  is negative. The vertical dashed lines highlight the 4 day (for wave 1) and 2 day (for wave 2) frequencies. The horizontal dotted line is at  $70^\circ\text{S}$ . Larger amplitudes are shaded.

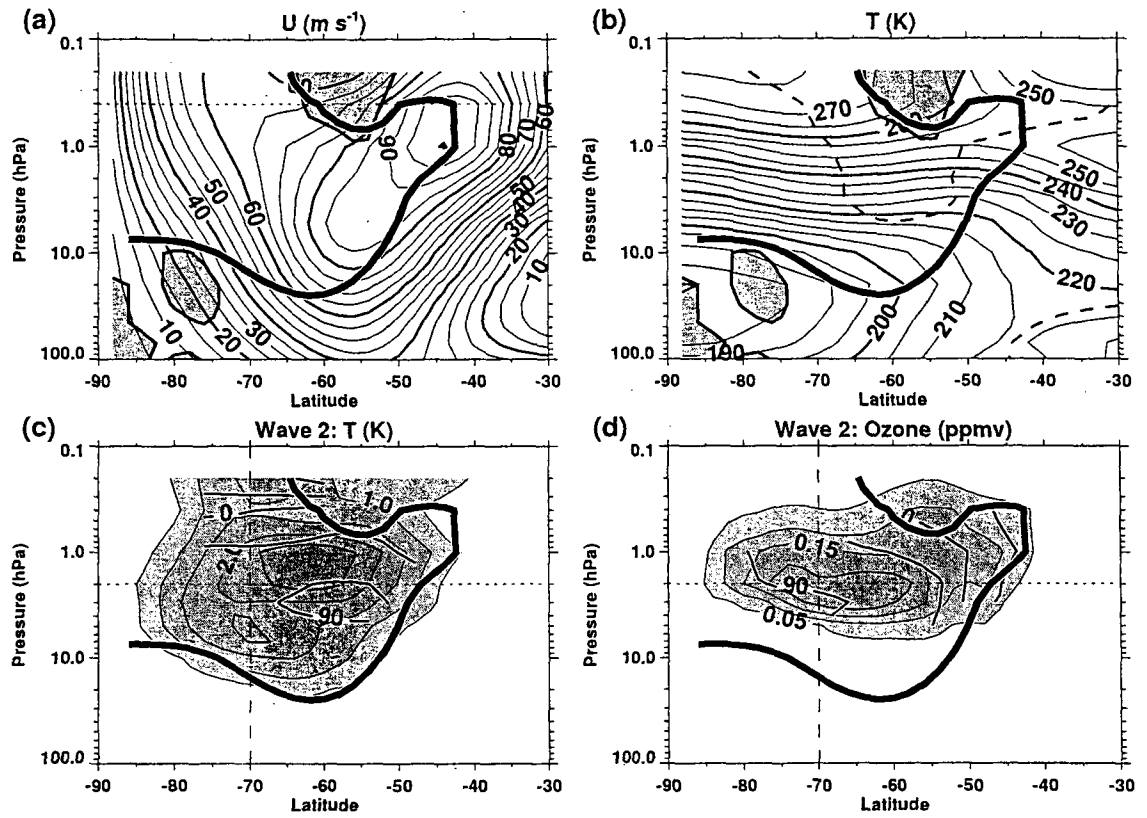


Figure 8: Wave 2 structure, July 1998, 1.72 day period, as a function of latitude and pressure. The heavy dark curve is the critical line. (a) zonal mean zonal wind ( $\text{m s}^{-1}$ ). Shaded region is where the zonal mean  $\text{pv}$  gradient,  $\bar{q}_y$ , is negative. Dotted reference line at 0.4 hPa (b) zonal mean temperature (K). Thicker dashed curve is where the horizontal temperature gradient is zero. Shaded region is where  $\bar{q}_y$  is negative. (c) temperature wave amplitude (K, shaded contours, contour interval 0.5 K) and phase (degrees, black lines, contour interval  $45^\circ$ ). (d) ozone wave amplitude (ppmv, shaded contours, contour interval 0.05 ppmv) and phase (degrees, black lines, contour interval  $45^\circ$ ). Reference broken lines at  $70^\circ\text{S}$  and 2 hPa in (c) and (d).

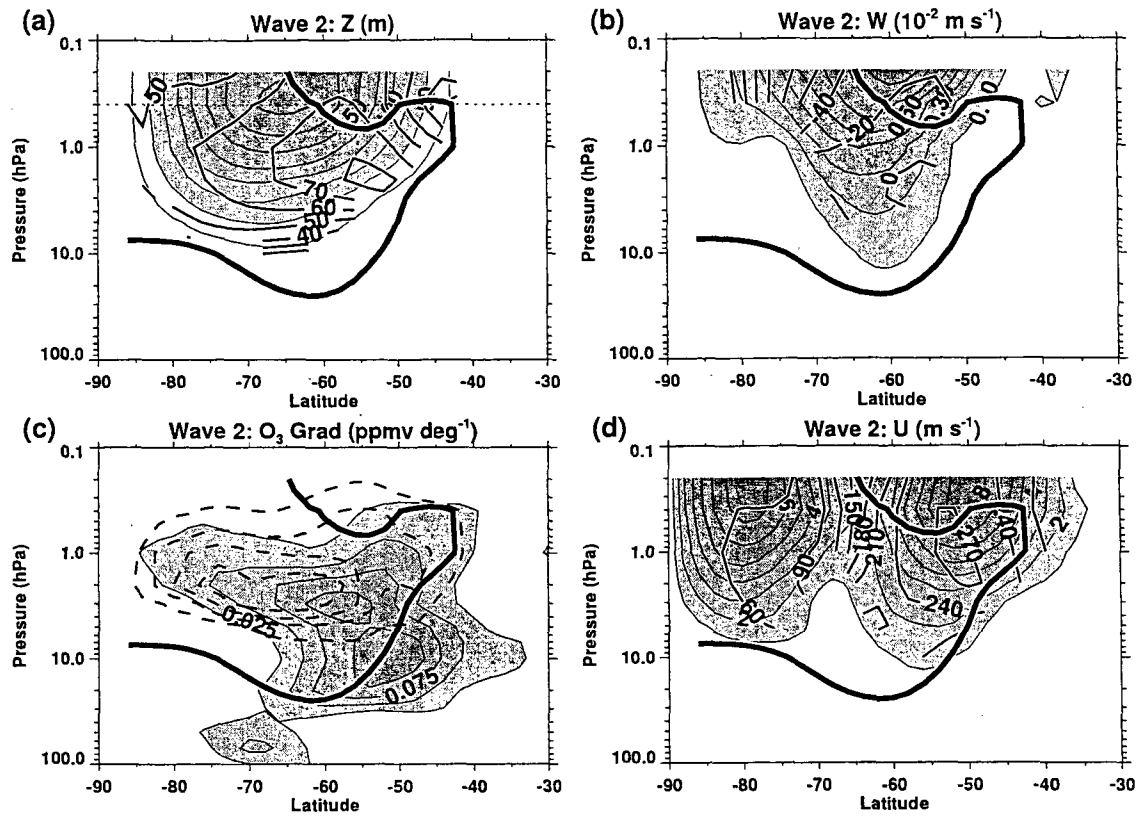


Figure 9: Wave 2 structure, July 1998, 1.72 day period, as a function of latitude and pressure. The heavy dark curve is the critical line. (a) geopotential height wave amplitude (m, shaded contours, contour interval 10 m, maximum contour is 80 m) and phase (degrees, black lines, contour interval 10°). Dotted reference line at 0.4 hPa; (b) vertical velocity amplitude ( $\times 10^{-2} \text{ m s}^{-1}$ , shaded contours, contour interval  $0.1 \times 10^{-2} \text{ m s}^{-1}$ ) and phase (degrees, black lines, contour interval 20°); (c) mean latitudinal ozone gradient ( $\text{ppmv deg}^{-1}$ , shaded contours, contour interval 0.025  $\text{ppmv deg}^{-1}$ ) and ozone wave amplitude (dashed lines) taken from Fig. 8d; (d) zonal wind amplitude ( $\text{m s}^{-1}$ , shaded contours, contour interval 1  $\text{m s}^{-1}$ ) and phase (degrees, black lines, contour interval 30°).

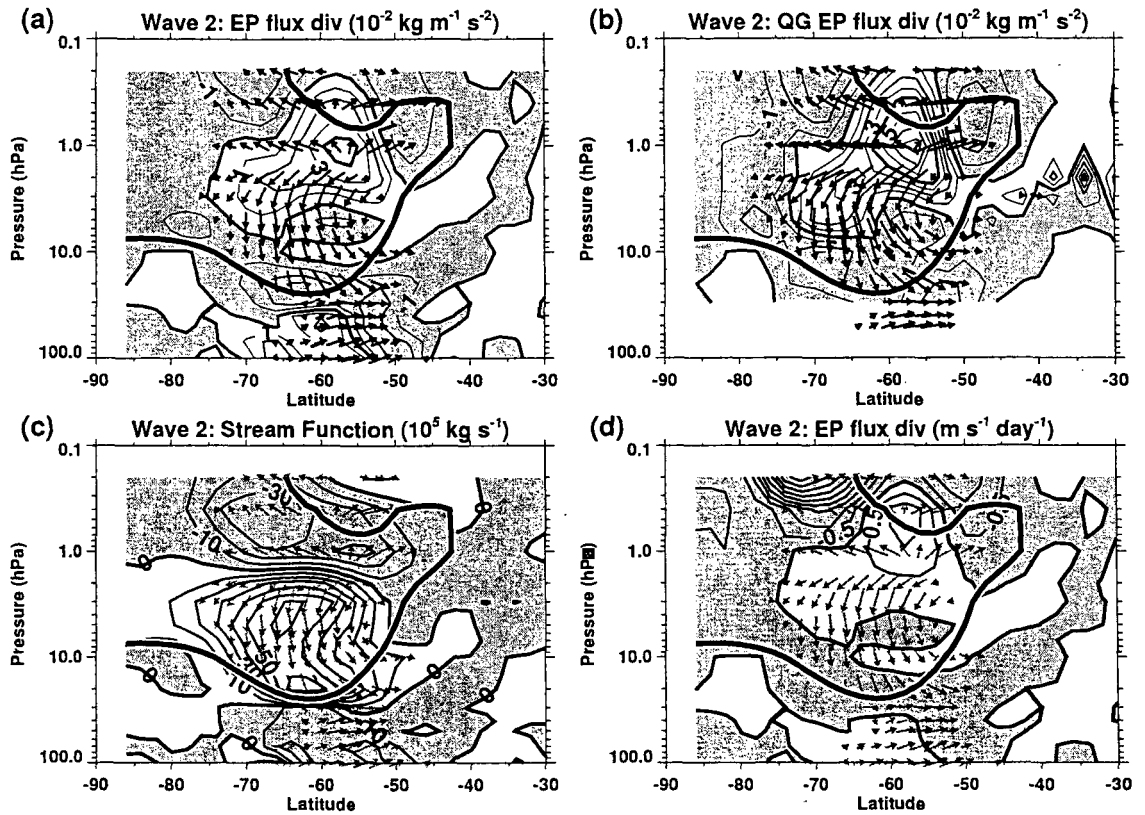


Figure 10: Wave 2 structure, July 1998, 1.72 day period, as a function of latitude and pressure. The heavy dark curve is the critical line. (a) EP flux divergence ( $10^{-2} \text{ kg m}^{-1} \text{ s}^{-2}$ ), negative values are shaded, contour interval  $10^{-2} \text{ kg m}^{-1} \text{ s}^{-2}$ , and arrows depict the EP flux vectors. (b) same as (a) except calculated from heights using quasi-geostrophic approximation. (c) wave-induced mass stream function ( $\times 10^5 \text{ kg s}^{-1}$ ), contours, negative values are shaded, contour interval  $10 \times 10^5 \text{ kg s}^{-1}$ ) and EP flux vectors from (a). (d) zonal mean wind forcing ( $\text{m s}^{-1} \text{ day}^{-1}$ , negative values are shaded, contour interval  $0.5 \text{ m s}^{-1} \text{ day}^{-1}$ ) and EP flux vectors from (a).

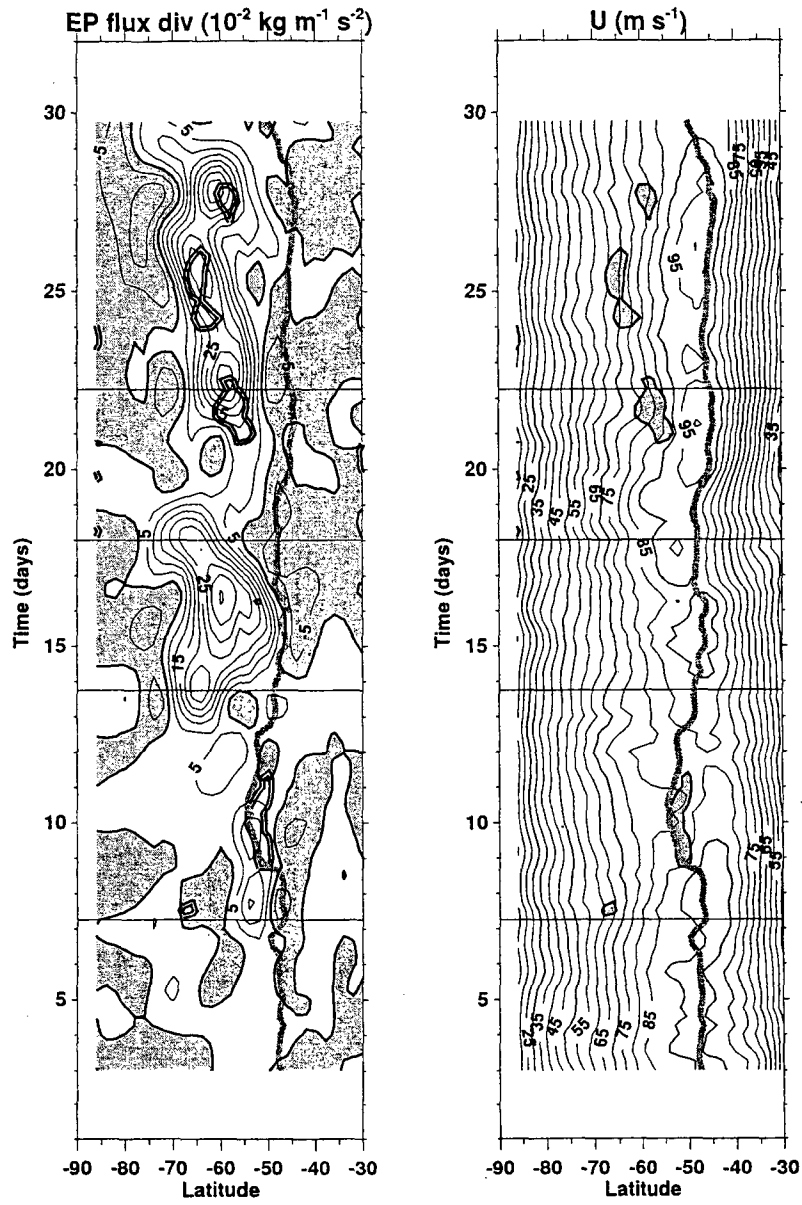


Figure 11: Time-latitude plots at 2 hPa for July 1998: (a) band pass filtered EP flux divergence ( $\times 10^{-2} \text{ kg m}^{-1} \text{ s}^{-2}$ ), contour interval  $5 \times 10^{-2} \text{ kg m}^{-1} \text{ s}^{-2}$ , negative values are shaded, negative  $\bar{q}_y$  regions double outlined. (b) zonal mean zonal wind ( $\text{m s}^{-1}$ ), contour interval  $5 \text{ m s}^{-1}$ , negative  $\bar{q}_y$  regions shaded. Thick gray line is the  $0.58 \text{ day}^{-1}$  critical line. The 4 horizontal lines correspond to the 4 times shown in Fig. 13.

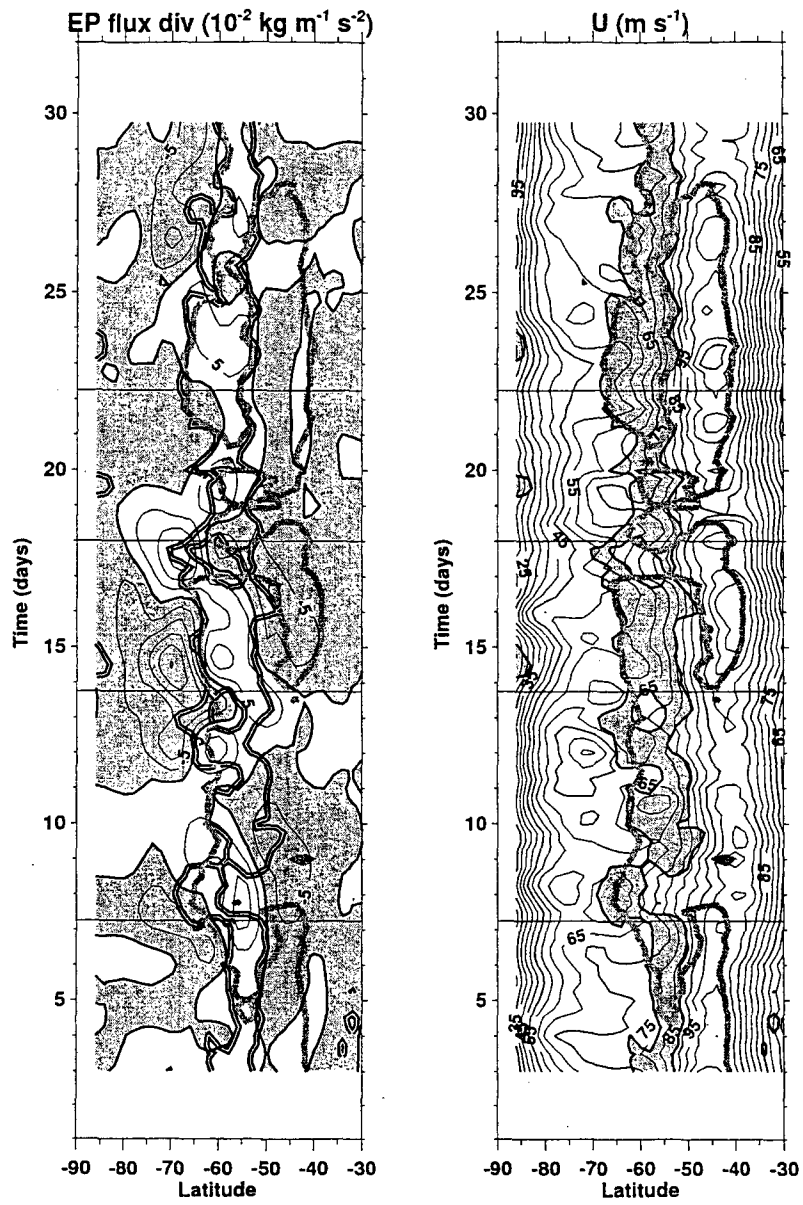


Figure 12: As in Fig. 11 but for the 0.4 hPa level.

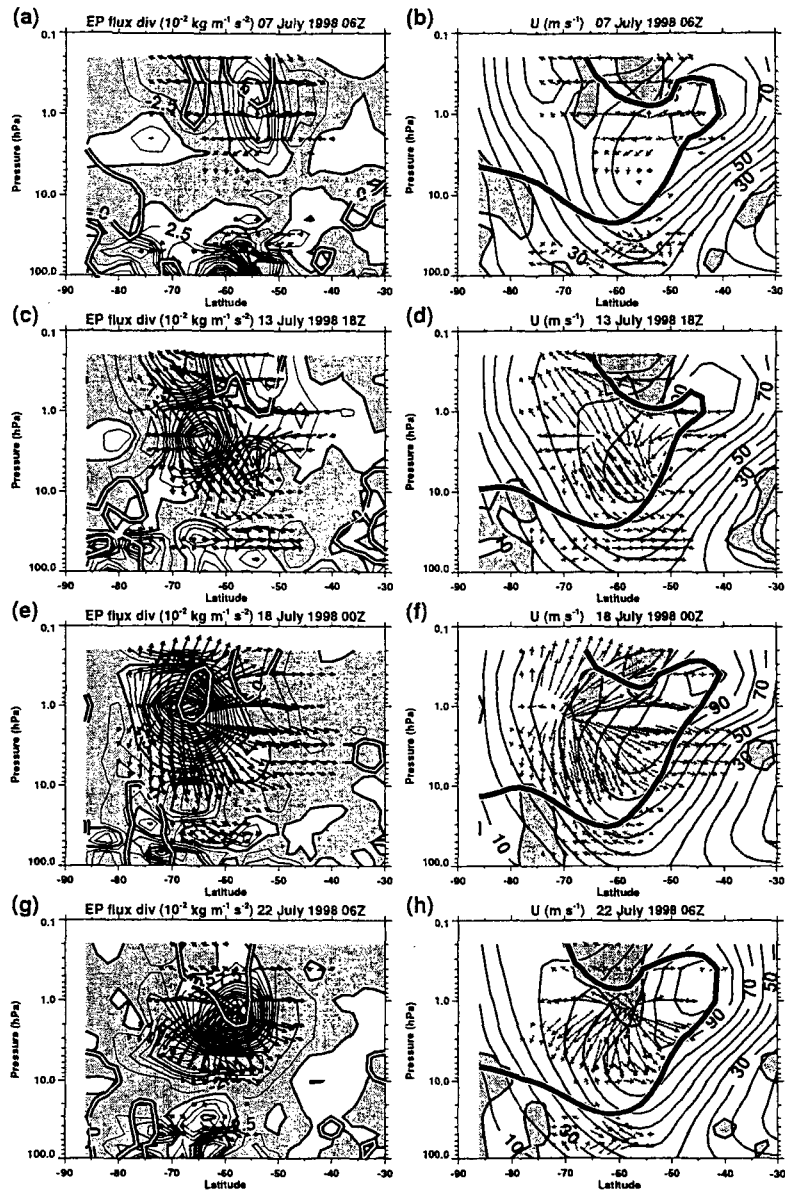


Figure 13: Plots of EP flux divergence (left, contour interval  $2.5 \times 10^{-2} \text{ kg m}^{-1} \text{ s}^{-2}$ , negative values are shaded) and zonal mean zonal wind (right, contour interval  $10 \text{ m s}^{-1}$ ) at four times during July 1998. EP flux vectors are scaled to be 40% smaller than in Fig. 10 to aid readability. The heavy line on the right is the critical line for a 1.72 day period wave 2 mode. Negative  $\bar{q}_y$  regions are shaded on the right and  $\bar{q}_y = 0$  are double lines on the left.

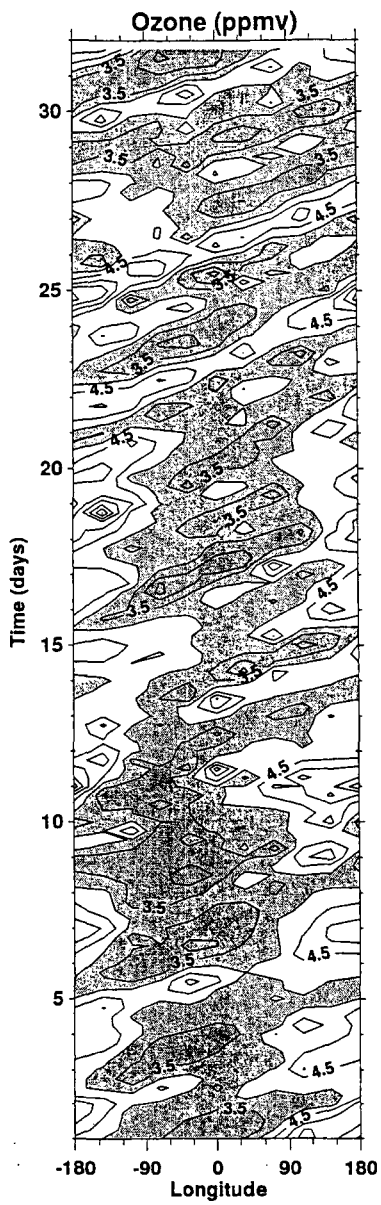


Figure 14: Longitude-time plot of POAM ozone (ppmv) at an average latitude of 68°S and 2 hPa for July 1998. Contour interval is 0.5 ppmv. Lower ozone values are shaded.

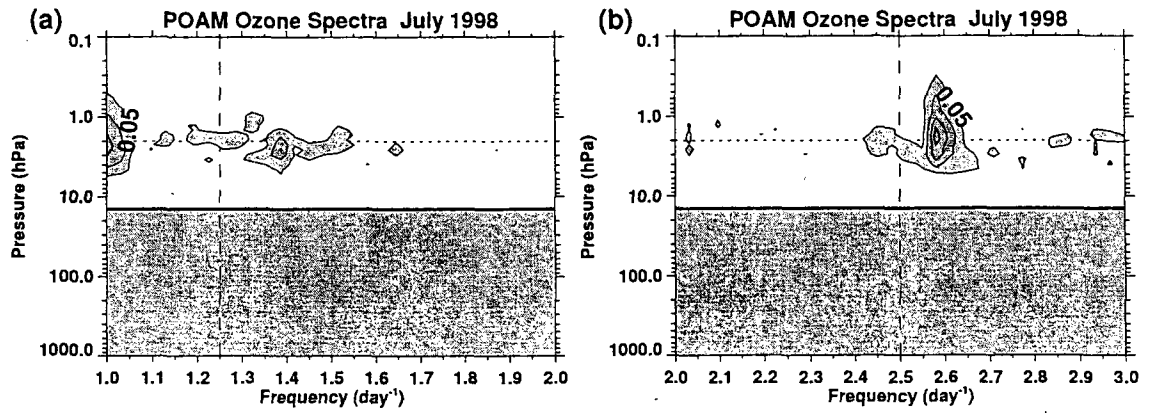


Figure 15: POAM ozone spectra (ppmv day) for July 1998 as a function of frequency and pressure: (a) for the frequency range 1–2 day<sup>-1</sup>, (b) for the frequency range 2–3 day<sup>-1</sup>. The contour interval is 0.05 ppmv. Higher values are shaded. The plot is split into two panels to aid in comparison with Fig. 5b and d, and corresponding reference lines are drawn. Only POAM observations above 14 hPa (heavy solid line) were analysed.